Skidmore College
Creative Matter

Chemistry Faculty Scholarship   Chemistry

2015

Photochemistry of Nitrate Chemisorbed on Various Metal Oxide Surfaces

Daniel Lesko
Skidmore College, dlesko@skidmore.edu

Ellen M. Coddens

Hannah Swomley
Skidmore College, hswomley@alumni.skidmore.edu

Rachel M. Welch

Jaya Borgatta
Skidmore College, jborgatt@skidmore.edu

See next page for additional authors

Follow this and additional works at: https://creativematter.skidmore.edu/chem_fac_schol

Part of the Chemistry Commons

Authors

Daniel Lesko, Ellen M. Coddens, Hannah Swomley, Rachel M. Welch, Jaya Borgatta, and Juan Navea

Volume 1 | Number 1 | Jan 2013 | Pages 1–100

PCCP

Physical Chemistry Chemical Physics
www.rsc.org/pccp

ROYAL SOCIETY OF CHEMISTRY

ROYAL SOCIETY OF CHEMISTRY

www.rsc.org/pccp

Photochemistry of Nitrate Chemisorbed on Various Metal Oxide Surfaces

Daniel M. B. Lesko,[a] Ellen M. Coddens,[b] Hannah D. Swomley,[a] Rachel M. Welch,[b] Jaya Borgatta,[a] and Juan G. Navea[a,*]

[a]*Chemistry Department, Skidmore College, Saratoga Springs, NY, 12866-1632*

[b]*Chemistry Department, Lawrence University, Appleton, WI, 54911*

* To whom correspondence should be addressed. Email: jnavea@skidmore.edu (J. Navea)

Atmospheric aerosols are known to provide an important surface for gas-solid interfaces that can lead to heterogeneous reactions impacting tropospheric chemistry. In this work, α-Fe_2O_3, TiO_2, γ-Al_2O_3, SiO_2 and ZnO, common components of atmospheric aerosols, served as models to investigate the gas-solid interface of nitric acid with aerosols in the presence of simulated solar radiation. Adsorbed nitrate and gaseous products can be continuously monitored with infrared spectroscopy (IR). Kinetic studies of adsorbed species were carried out using attenuated total reflectance infrared spectroscopy (ATR-FTIR). *Ex-situ* simultaneous infrared spectroscopy of gas-phase products using a 2 m long path cell allowed the detection of gaseous products at early stages of the heterogeneous photochemical reaction. In addition, photoactive gaseous products, such as HONO, were detected as gas analysis was carried out outside the region of irradiation. All reactions were found to be first order with respect to adsorbed nitric acid and yielded gas-

phase products such as NO, NO_2, N_2O_4, N_2O, and HONO. While the correlation between semiconductor properties of the metal oxide and the heterogeneous photochemical rate constant (*j*) is not direct, the semiconductor properties were found to play a role in the formation of relatively high proportions of greenhouse gas nitrous oxide (N_2O).

I.   Introduction

Particulate matter, a significant component of the atmosphere in both urban and remote areas, is known to provide an active surface where tropospheric gases can undergo heterogeneous chemical reactions.[1-4] Over the last decade it has become clear that heterogeneous chemistry and photochemistry with solar radiation play an important role in the chemical balance of the atmosphere.[1,5-8] As a result, heterogeneous mechanisms with important climate implications are now being proposed. For example, several studies suggest that the reaction of mineral dust aerosol with nitric acid, a known atmospheric sink of nitrogen oxides, may have a significant impact in the renoxification of the troposphere.[2,9-13] These heterogeneous processes are rather complex and closely dependent on aerosol composition, which varies broadly as it depends on the source of the aerosol event.[2,9,14-19] Consequently, in order to better understand the heterogeneous effect of aerosols in the renoxification of the troposphere it is important to understand the role of each component of particulate matter in the heterogeneous chemistry of nitric acid.[20]

Among the components of tropospheric particulate matter are photoactive species such as semiconductor metal oxides that can play a determining role in the kinetics, formation of reaction products, and product yields of adsorbed nitrate photochemistry. In fact, species like TiO_2 and Fe_2O_3, with bad-gaps smaller than the cutoff of solar radiation in the troposphere, can reach over 4% by mass in an aerosol formed during dust events.[21,22] Even if these species are relatively minor components of tropospheric mineral aerosols, they can have an important impact in daytime chemistry. Recently, several studies suggest that these types of semiconductor metal oxides can initiate further photochemical reactions on their surfaces, with important implications in the kinetic and product formation of heterogeneous photochemical processes. For instance, the

heterogeneous decomposition of O_3 on Fe_2O_3 has shown significant photoenhancement.[2] In addition, species with no photoactive properties have been shown to induce daytime chemistry through surface effects. In fact, recent studies on the heterogeneous photochemistry of nitric acid on alumina, a component of mineral dust, determined that a significant fraction of adsorbed nitrate reacted in the presence of solar radiation to form NO_x and green-house gas N_2O.[10,23] Therefore, it is important to establish the effect of photoactive and non-photoactive components of aerosol in photochemical reactions.

Laboratory studies have shown that most photochemical decomposition of chemisorbed nitrogen oxides under broadband radiation takes place during the first two hours of irradiation.[10,23] While infrared spectroscopy has proven efficient in determining the removal of chemisorbed species, the spectroscopic analysis of gas-phase products is more challenging because many proposed intermediate species, such as nitrous acid (HONO), are photoactive. As a result, the gas-phase analysis in traditional single-vessel reactors, where products are continuously exposed to solar radiation, are ineffective to provide direct evidence of HONO formation. In addition, products with low molar absorptivity have only been observed after several hours of irradiation and product accumulation. In order to achieve high sensitivity in gaseous product analysis and compare kinetics and yields of the photochemical reactions of nitric acid adsorbed on aerosol particles, we carried out photochemical studies of adsorbed nitrate on components of mineral aerosol, hematite (α-Fe_2O_3), anatase (TiO_2), alumina (γ-Al_2O_3), silica (SiO_2) and zinc oxide (ZnO), under simulated solar radiation at the same time that gas phase products are investigated in an *ex situ* 2 meters long-path-cell coupled with the photochemical reactor system.

II. Experimental Section

Five commercially available powders were used in this study: γ-Al$_2$O$_3$ (Degusa, Aluminum oxide C), TiO$_2$ (Aldrich), α-Fe$_2$O$_3$ (Aldrich), ZnO (Essential Depot), and SiO$_2$ (Stream Chemicals). All of these oxides are relevant components of tropospheric aerosols with contrasting photoactive properties; while TiO$_2$, ZnO, and α-Fe$_2$O$_3$ are semiconductive materials with band gaps energies below the cutoff of solar radiation at the top of the atmosphere, γ-Al$_2$O$_3$ and SiO$_2$ are well known insulators. Surface areas of all oxide samples were determined by a seven-point N$_2$-BET adsorption isotherm using a Quantachrome Nova 2200e surface area analyzer. The surface areas are (99.2 ± 0.5) m^2 g^{-1}, (54.99 ± 0.04) m^2 g^{-1}, (23 ± 2) m^2 g^{-1}, (5.7 ± 0.4) m^2 g^{-1}, and (4.06 ± 0.05) m^2 g^{-1} for γ-Al$_2$O$_3$, TiO$_2$, α-Fe$_2$O$_3$, ZnO, and SiO$_2$ respectively.

There are three main components to the experimental setup (Figure 1): the gas generator, the photochemical cell, and the gas analysis chamber.
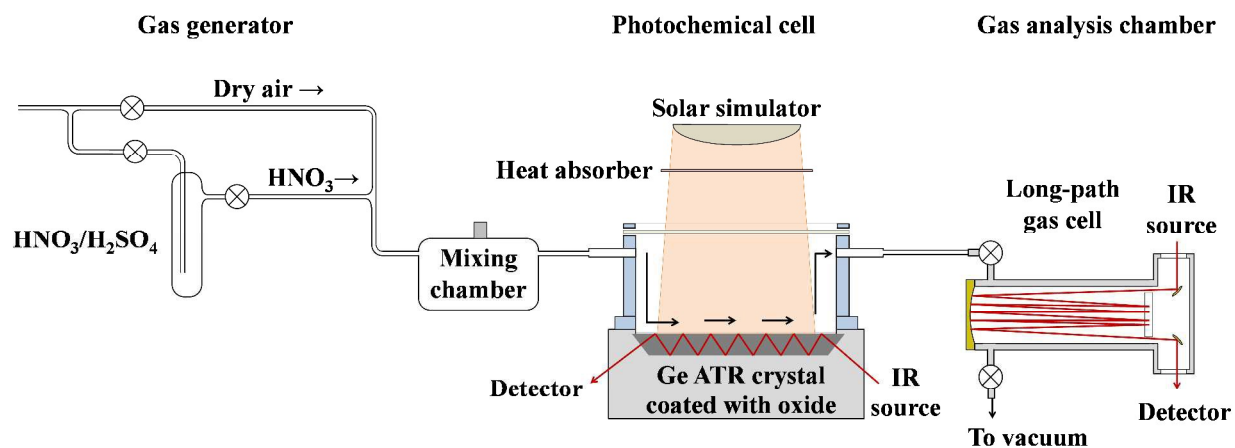
Figure 1. Schematic diagram of the experimental set-up used in these studies.

To generate the gaseous HNO$_3$ and carry it into the reaction photochemical cell, a flow of purified dry air with a relative humidity <1% was bubbled through a 3:1 mixture of sulfuric acid

(96.0%) and nitric acid (79.5%), and the resulting nitric acid gas was flowed to the photochemical cell.

The photochemical cell consists of a Teflon chamber enclosing a 72 × 4 mm attenuated total reflection (ATR) germanium crystal (Pike Technologies), which supports the metal oxide sample to be studied. A UV-Vis transmission window (Ultran®) on top of the Teflon chamber allows broadband irradiation of the metal oxide sample and removes radiation below 290 nm. Finally, the photochemical cell is coupled to a Fourier Transformed infrared (FTIR) spectrometer (Thermo, 6700) for continuous ATR-FTIR analysis. The photochemical cell reaction chamber (54.0 cm^3) contains a gas inlet and outlet to allow coupling with a sample/vacuum line and an IR long-path cell for gas-phase product analysis. The vacuum line consists of a mechanical vacuum with pressure transducers and ports for gas introduction. As shown in Figure 1, the photolysis of adsorbed nitrate compounds is carried out in the reaction photochemical cell. A broadband light source (ORIEL, 500 W) is placed on top of the photochemical cell. Light passes through a heat absorber filter to remove infrared radiation and prevent a temperature rise in the photochemical cell. As adsorbed nitric acid photolysis takes place, gaseous products desorb and diffuse out of the irradiation region and towards the gas analysis chamber.

The gas analysis chamber is a 200.0 cm^3 IR long-path cell (Thermo), which consists of a 2 meter optical path with barium fluoride windows and gold coated optics. The volume of the tubing connecting the photochemical cell with the long-path cell is considered negligible. The cell is in a second Fourier Transformed infrared (FTIR) spectrometer (Thermo, iS50) for continuous gas-phase analysis, which is performed simultaneously with the surface analysis in the photochemical cell.

In a typical experiment, the formation of the oxide film was carried out by preparing a slurry of the oxide powder and applying it onto the ATR crystal; as the slurry evaporates, a thin film of the metal oxide was deposited on the surface of the ATR crystal, resulting in a visually homogeneous metal oxide film. Only the γ-Al_2O_3 film was prepared by pressing the powder onto the Ge crystal surface. Once in the cell, the oxide film was dried under vacuum overnight.

Following the overnight drying of the ATR crystal coated with the oxide film, gaseous HNO_3 was introduced into the photochemical reaction cell in order to adsorb nitric acid onto the oxide surface. Using the spectra of the dry oxide as a reference, nitric acid adsorption on the oxide surface was continuously monitored throughout the adsorption process by collecting infrared spectra, where adsorbed nitrates show absorption bands in the region 1700 to 1100 cm^{-1}.[24] The flow of nitric acid over the oxide surface continued until the surface nitrate features stopped growing, indicating surface saturation. Following an overnight evacuation, the resulting surface was consider saturated with chemisorbed nitrate, and the integration of the chemisorbed nitrate absorption bands was set as the initial surface coverage (θ_0).

In a typical experiment, infrared scans are recorded under vacuum and dark conditions for over 30 minutes to quantify any non-photocemical/heterogeneous reaction by monitoring changes in the adsorbed nitrate and any gas-phase product in the long-path cell. After this baseline time, the broadband light source ($\lambda > 300$ nm) is turned on to begin the photochemical reaction (t = 0 minutes), which is allowed to proceed under vacuum for at least 350 minutes. During irradiation, the ATR-FTIR spectra of the nitrated surface are recorded every 2 minutes to allow kinetic analysis. Simultaneously, gas phase products are detected with the FTIR long-path cell with the

same time intervals. Typically, 240 scans of 4 cm^{-1} resolution are collected for both surface chemisorbed nitrate and gas-phase products.

The partial pressures of gas-phase species were determined using a Beer's law calibration with NO$_2$, NO, and N$_2$O standards (Sigma-Aldrich) with 99.5, 98.5 and 99% purity respectively. Gas standards were introduced into the long-path cell through a vacuum line after the cell was evacuated. The absorbance of each gas was recorded separately at several different pressures. For the gas products observed, the absorbance was determined and found in good agreement available literature values.[2,23] The NO absorbance in the spectral region between 1973 and 1880 cm^{-1} was determined to be 0.1955 Torr^{-1}; the N$_2$O absorbance in the spectral region between 2263 and 2143 cm^{-1} was 3.7347 Torr^{-1}; the NO$_2$ absorbance in the spectral region between 1660 and 1550 cm^{-1} was 7.5256 Torr^{-1}. The limits of detection for NO$_2$ and N$_2$O and NO were 2, 2, and 5 mTorr respectively. The partial pressure of HONO was determined from previously reported cross sections,[25, 26] while the partial pressure of N$_2$O$_4$ was calculated from the known equilibrium constant between this gas and its monomer, NO$_2$.

Diffuse-reflectance UV-Vis spectroscopy (DRS UV-Vis) studies of the metal oxides examined were performed using a Lambda 35 Spectrophotometer (Perkin Elmer) equipped with an integrating sphere. In order to evaluate the semiconductor properties of the oxide samples, all spectra were referenced to 100% reflection. The DRS UV-Vis referenced to 100% reflection was used to calculate the band-gap of the powders in the spectral region between 200 and 1100 nm. The calculated band-gap for TiO$_2$, ZnO, and α-Fe$_2$O$_3$ are (3.07 ± 0.01) eV, (3.10 ± 0.03) eV, and (2.24 ± 0.02) eV, respectively. These values are in good agreement with reported literature values.[27]

III. Results and Discussions

3.1 Irradiance Profile in the Photochemical Cell. The spectral absolute irradiance was determined by placing a calibrated spectroradiometer (Oriel USB4000) at the ATR crystal level, a distance approximately 17 cm from the broadband light source and at the highest intensity region of the broad-band light beam. The UV-Transmission window on the photochemical cell effectively blocks radiation below 290 nm, a threshold wavelength above which the absolute irradiace sharply increases. Spectral profile in the region of interest are shown in Figure 2A, along with the absorption cross-sections for NO_2 and HONO, the two photoactive species with overlap between the light source and the absorption profile. Figure 2B represents the spatial distribution of the light source beam at the level of the ATR crystal, where heterogeneous photochemistry takes place. The broadband light intensity distribution was measured across the ATR crystal using a calibrated photocell. The light intensity shows a Gaussian profile, with obscuration effects at each end of the crystal. At the center of the crystal, the irradiance of the light beam has an average output of approximately 1.10 kW m^{-2}, or 1.2 of air mass 1 (AM1), similar to the irradiance at the top of Earth's atmosphere. Overall, the region of irradiation has a diameter of approximately 5 cm. As indicated above, this irradiance output is kept constant through the experiment. In addition, a heat absorber filter (Newport) is used to remove infrared radiation and maintain isothermal conditions throughout the experiment.

A

B
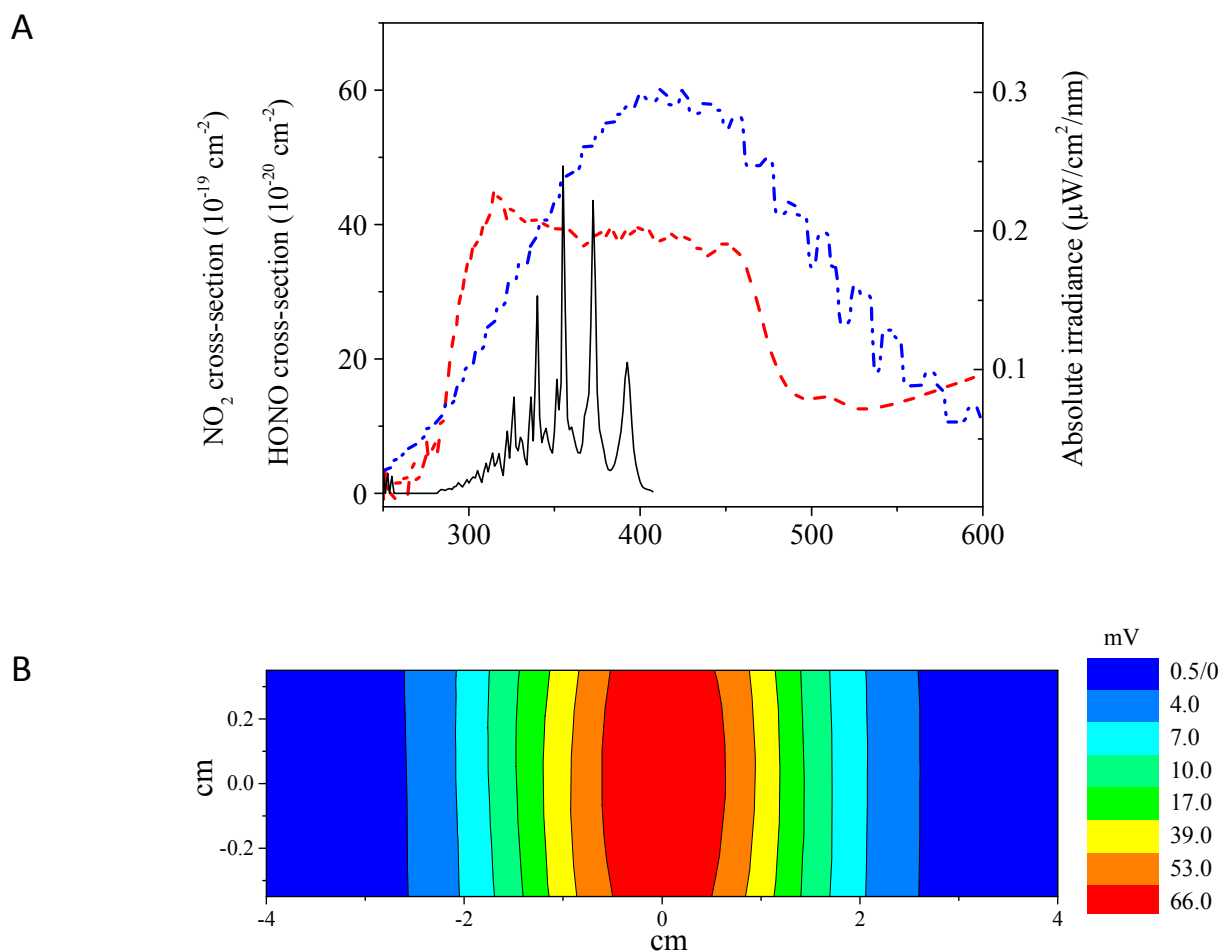
Figure 2: (A) Solar simulator spectral irradiance (dashed red line) at the bottom of the photochemistry cell. As a reference, the absorption cross sections of nitrous acid (solid black line), nitrogen dioxide (dashed-dotted blue line) are also shown. (B) Solar constant profile in the chamber at the ATR crystal. The total area of irradiance shows a Gaussian profile with a radius of approximately 5 cm at the ATR crystal level.

3.2 Vibrational spectroscopy of photochemical reaction. An overview of the heterogeneous photochemical reaction of chemisorbed nitric acid on five different oxide surfaces is presented in Figure 3, where panel A shows the spectra on the surface (photochemical cell), and panel B shows the spectra in the gas phase (gas analysis chamber).
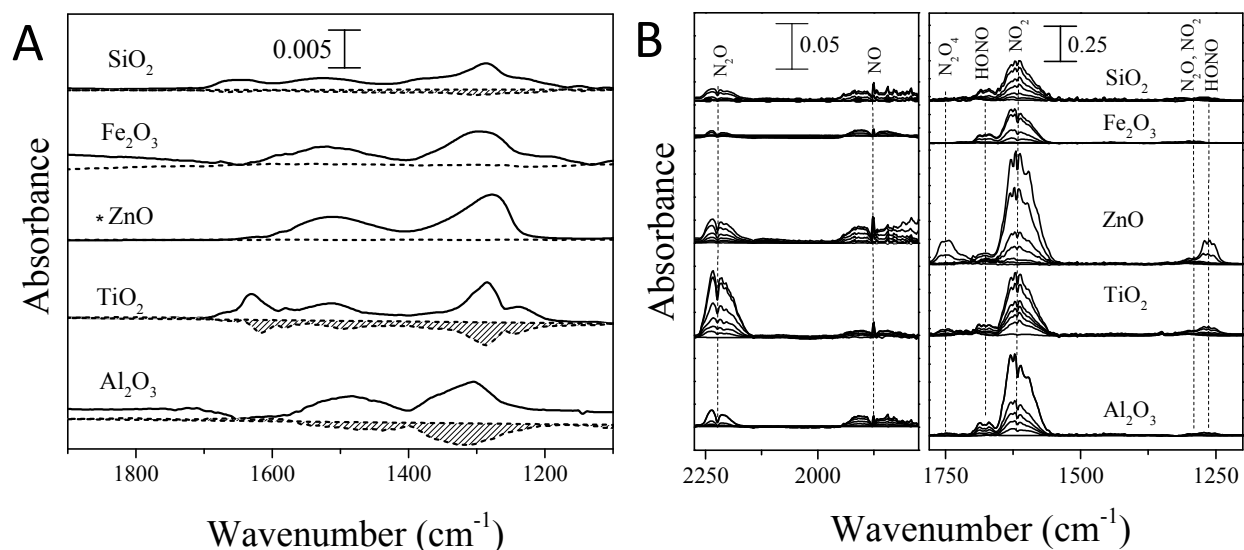
Figure 3. (A) Attenuated total reflection–Fourier transform infrared (ATR-FTIR) spectra of surface adsorbed nitrate. The solid line represents the reaction before irradiation (t=0) and the dashed line with the filled area represents the difference between the spectral data at time t=350 min and t=0 min.   The * indicates that the scale for ZnO is shown 20 times smaller than measured for purpose of presentation. (B) Time progression of gas-phase products– a scan before irradiation, 10 minutes after irradiation, and then subsequent FTIR scans with 90 minutes intervals. Five different surfaces are shown: γ-Al_2O_3, TiO_2 (anatase), ZnO, α-Fe_2O_3, SiO_2.

Figure 3A displays the infrared spectra for chemisorbed nitric acid, where the broken line with filled area represents the fraction of nitric acid loss from the surface relative to t = 350 min which is represented as the difference between the absorbance at 350 min of irradiation, Abs_{350}, and the absorbance before irradiation, Abs_0, $(Abs_{350} - Abs_0)$. The multiple features observed in the infrared spectra correspond to different modes of coordination of nitrates with the oxide surface.[23,24,29] Two common vibrational absorption bands for chemisorbed nitrate, with slight shifts caused by surface-nitrate coordination on the different surfaces tested, are observed in the

spectrum collected before irradiation (solid line). An intense absorption band between 1304 and 1286 cm^{-1} and a less intense absorption band between 1523 and 1483 cm^{-1} can both be assigned to asymmetric N-O stretch of different coordinations of adsorbed nitrate. The HNO_3 chemisorbed on TiO_2 shows an intense absorption band at 1622 cm^{-1}, also corresponding to an asymmetric N-O stretch. This feature is smaller, but observable in all the oxide surfaces examined.

While most of the oxides examined will coordinate nitrate ion with the metal, ZnO and SiO_2 show a distinctive adsorption mechanism. The hydroxyl termination of the SiO_2 surface leads to a chemisorption of molecular nitric acid through hydrogen bonding interaction.[30] While all the powders have acid and base surface sites, SiO_2 is classified as a non-reactive neutral powder, and γ-Al_2O_3, α-Fe_2O_3, and TiO_2 are amphoteric reactive-insoluble powders.[31,32] On the other hand, ZnO is the only reactive basic powder examined. [30,31] As a consequence, it is expected that a significant fraction of ZnO surface will react upon interaction with HNO_3. Significantly, the relatively stronger absorption bands observed on ZnO surface implies a larger nitrate surface concentration resulting from a neutralization reaction with the subsequent formation of the nitrate salt. In fact, vibrational bands at 1308, 1025, 799 cm^{-1} (not shown in Figure 3A) can be assigned to a nitrate salt ν_3 symmetric stretch, ν_1 symmetric stretch, and ν_2 out-of-plane bend, respectively, while the vibrational band at 1518 cm^{-1} is assigned to ν_3 symmetric stretch of nitrate chemisorbed on metal oxides.[33] It has been suggested that this heterogeneous reaction to form $Zn(NO_3)_2$ follows a two-step mechanism: $ZnO + HNO_3 \rightarrow Zn(OH)NO_3 + HNO_3 \rightarrow Zn(NO_3)_2 + H_2O$.[30] Here, adsorbed water is lost from the surface after overnight vacuum. Overall, this suggests that, for experiments on ZnO surfaces, nitrate salt and chemisorbed nitrate are present.

Figure 3A indicates that surface nitrate is lost from γ-Al_2O_3 and TiO_2 in a larger proportion than any other surface examined. A smaller, but measurable loss of chemisorbed nitric acid is also observed on SiO_2 and ZnO. However, from surface infrared spectra there is no clear evidence of nitrate loss after 350 minutes of irradiation on α-Fe_2O_3. It is especially clear from the HNO_3 removed from the TiO_2 surface that a few features of the chemisorbed nitrate are preferentially removed from the surface, suggesting that not all the nitrate-oxide coordination structures will undergo heterogeneous photolysis.[23]

As indicated above, gas-phase products diffuse out of the reaction photochemical cell and are analyzed in the absence of broadband radiation during the progress of the photochemical heterogeneous reaction. Figure 3B shows representative FTIR spectra of the long-path cell at different stages of the photochemical reaction, where the content of the long-path cell can be analyzed based on the increase of absorption bands. Figure 3B represents the time progression of the gas-phase experimental IR data, where the six spectra displayed correspond to the gas phase: a scan before irradiation, 10 minutes after irradiation, and then subsequent FTIR scans with 90 minute intervals. No significant absorption bands were observed to grow under dark conditions. More noticeable, from Figure 3B it is evident that all surfaces examined induce photochemical heterogeneous reactions to some extent, as absorption bands of gas-phase species are observed to grow with irradiation time for all five surfaces. It must be noted that Figure 3B shows the total amount of gaseous product; this amount depends on the initial coverage of chemisorbed nitric acid, which varies for each surface. In section 3.3 we discuss the gas-phase products relative to the initial coverage of nitric acid.

Figure 3B shows several absorption bands: three of these bands, centered at 1616, 1878, 2221 cm^{-1}, are attributed to NO_2, NO, and N_2O respectively.[2] In addition, a vibrational band observed at 1749 cm^{-1} corresponds to the nitrogen dioxide dimer N_2O_4. Finally, a fifth band centered at 1678 cm^{-1} is observed, particularly strong for the photochemical reaction on α-Fe_2O_3, TiO_2, and γ-Al_2O_3, although still observable for all the oxides examined. This fifth band is attributable to the fundamental ν_2 vibrational mode of nitrous acid, HONO.[34] In addition, a small, but observable band centered at 1263 cm^{-1} can also be assigned to the fundamental ν_3 vibrational mode of HONO.[25,34]

All the infrared absorption bands of the gas-phase products were observed to grow with respect to irradiation time of the nitrated surface. In the case of γ-Al_2O_3, TiO_2, SiO_2, and ZnO all the gas-phase infrared features increased as the surface nitrate decreased. Simultaneously, growth of gas-phase products is observed for α-Fe_2O_3, even though there was no observed loss of chemisorbed nitrate from this surface. This discrepancy can be attributed to the larger sensitivity of the long-path gas cell compared to the sensitivity of the ATR in the photochemical cell. It is important to point out that, from all gas-phase products observed during the heterogeneous photolysis of nitrate on SiO_2, only NO_2, N_2O and NO were above the limit of quantification of the experiment. No quantifiable concentrations of HONO were quantified from the SiO_2 surface.

3.2 Kinetics of surface nitrate photochemistry. Analysis of the area of the absorption bands before irradiation indicates that there is no significant loss of surface nitrates in the absence of light. In addition, no significant gas-phase products are observed in the absence of broadband irradiation. Upon irradiation, the infrared spectra of chemisorbed nitrate on each oxide surface were recorded. In all cases where nitrate loss was measured, an exponential removal was

observed for the first several minutes of broadband irradiation, suggesting first order reaction kinetics. The chemisorbed nitrate loss is analyzed relative to the initial entire normalized nitrate absorbance region before irradiation, which for analysis purposes is defined as the initial nitrate surface coverage (θ_0). Figure 4A shows the relative loss in the surface nitrate with respect to irradiation time, over several hours of experiment, for all the oxides examined.
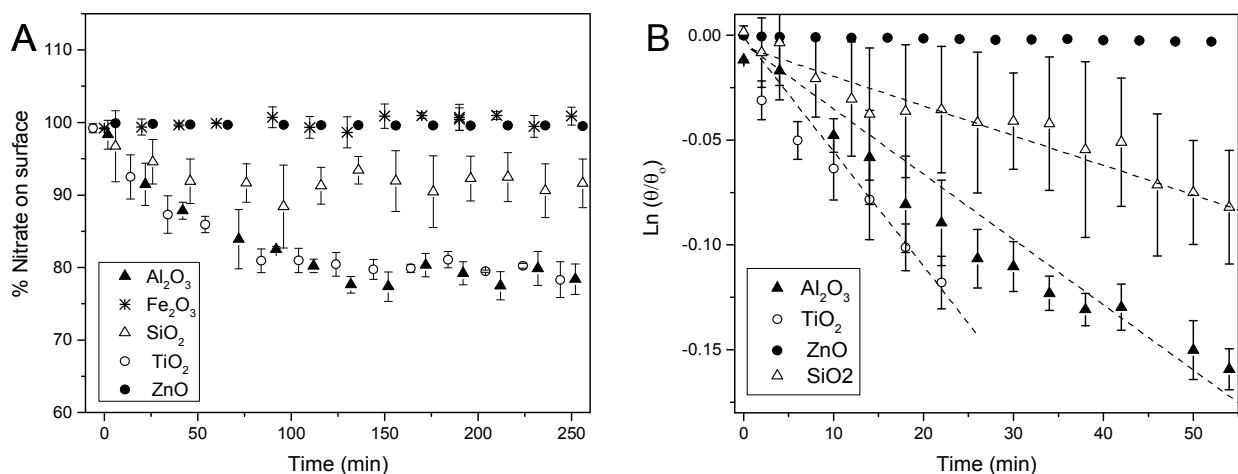
Figure 4. Photochemical loss of chemisorbed nitrate on different oxide surfaces. Measurements are referenced to the nitrate saturated surface at t=0 minutes (θ_o). Panel A shows chemisorbed nitrate loss; each point is the mean of at least triplicate measurements and the error bars represent the standard deviation. Panel B shows the natural logarithm of the removed nitrate fraction. The dotted line represents the linear regression over the first order kinetics regime used to delimit the exponential decay of surface nitrate. For clarity, only 12% of the data are plotted.

From Figure 4A, exponential loss on γ-Al_2O_3 and TiO_2 was observed, with a percentage of chemisorbed nitrate loss ($\left[\frac{\theta}{\theta_0} - 1\right] \times 100$) over 350 minutes of reaction of $(27 \pm 3)\%$ and $(18 \pm 4)\%$, respectively. In addition, SiO_2 also shows an exponential loss of chemisorbed nitrate in to
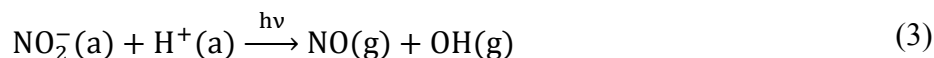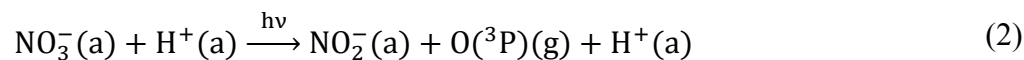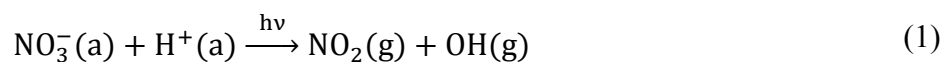
lesser extent, with surface nitrate loss of $(9 \pm 4)\%$ over 350 minutes of broadband irradiation.

ZnO, although not apparent from Figure 4A, also shows an exponential removal of chemisorbed

nitrate; however, because of its neutralization reaction (*vide supra*) the percentage of

chemisorbed nitrate loss on ZnO throughout the experiment is only (0.5 ± 0.2) %. Note that

nitrate loss in ZnO experiments can be due to a combination of chemisorbed nitrate and

$Zn(NO_3)_2$. The time frame of the exponential removal is determined by the limit of linearity

(LOL) of the natural logarithm of the adsorbed nitrate fraction, as shown in Figure 4B. The

percent loss of chemisorbed nitrate as a function of irradiation at the end of the exponential loss

(ϕ_{LOL}) as well as the loss of nitrate after 350 minutes of irradiation (ϕ_{350}) is reported in Table 1.

Overall, no absorption bands were observed to grow on the irradiated surface. However,

formation of surface-bound nitrite (NO_2^-) on γ-Al_2O_3 and NO^- on α-Fe_2O_3 has been reported in

recent experiments.[9,23]

Table 1. First-order photolysis rate constants (*j*), photochemical reaction yields at the limit of

linearity (ϕ_{LOL}), limit of linearity (LOL), and photochemical reaction yields at 350 minutes of

reaction (ϕ_{350}) of chemisorbed nitrate on different oxide surfaces. Data presented are averages of

triplicate measurements.

Surface	ϕ_{LOL} (%)	$j \times 10^{-5}$ (s^{-1})	LOL ± 2 (min)	ϕ_{350} (%)
γ-Al_2O_3	15 ± 1	4.4 ± 0.2	54	27 ± 3
TiO_2	10 ± 3	7.6 ± 0.2	24	18 ± 4
ZnO	0.35 ± 0.09	0.058 ± 0.003	74	0.5 ± 0.2
α-Fe_2O_3	< LOD	< LOD	N/A	N/A
SiO_2	7 ± 5	2.3 ± 0.1	54	9 ± 4

LOD = Limit of detection

The larger loss of chemisorbed nitrate on γ-Al$_2$O$_3$ and TiO$_2$ (ϕ_{LOL} and ϕ_{350} in Table 1) can be attributed to varying nitrate-oxide coordination, which is inherently different in each oxide and should result in a change in the electronic structure and chemical potential of chemisorbed nitrate.[17,35,36] As a chromophore, adsorbed nitrate will absorb photons that can induce photodissociation reactions with a mechanism similar to that of aqueous nitrate (equations 1, 2 and 3).[10,23,37]

$$NO_3^-(a) + H^+(a) \xrightarrow{h\nu} NO_2(g) + OH(g) \tag{1}$$

$$NO_3^-(a) + H^+(a) \xrightarrow{h\nu} NO_2^-(a) + O(^3P)(g) + H^+(a) \tag{2}$$

$$NO_2^-(a) + H^+(a) \xrightarrow{h\nu} NO(g) + OH(g) \tag{3}$$

where (a) represent adsorbed species. Gases NO and NO$_2$ were observed as products of the reaction and will continue to react, leading to the formation of the additional gas products observed in Figure 3B. The formation of N$_2$O has been proposed in previous studies through two possible mechanisms, the first one is a one-step mechanism shown in equation (4):[38]

$$NO_3^-(a) + NO_2(g) \rightarrow N_2O(g) + \frac{7}{4}O_2(g) + \frac{1}{2}O^{2-}(g) \tag{4}$$
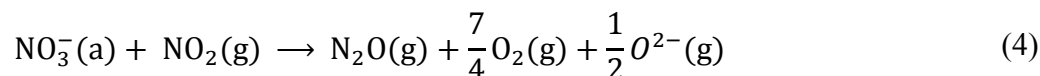
Alternatively, Beaumont and collaborators proposed a mechanism for the formation of HONO through a surface nitrate reduction process similar to equation (2), followed by a photoinduced desorption of nitrous acid.[40,41] This mechanism, supported by the observation of adsorbed NO$_2^-$,[34] is also supported by the absorption bands attributable to HONO.

In addition to the chromophore properties of the substrate, TiO_2 (anatase) is a well-known semiconductor, implying an additional photochemical activity. In general, the TiO_2 band gap energy is 3.07 eV (corresponding to 404 nm),[27] well above the cutoff of our solar simulator under experimental conditions (290 nm). Thus, irradiation of TiO_2 with photons having energies higher than 3.07 eV can create electron-hole pairs. As long as the thermodynamic potential of the chemisorbed nitrate is below the conduction band of TiO_2, a photochemical surface-induced reaction can be initiated. Thus, the loss of chemisorbed nitrate from TiO_2 can be a combination of light absorption and dissociation by the substrate and a surface reaction induced by the electron-hole pairs. Both, α-Fe_2O_3 and ZnO are also semiconductors with band gaps energy measured at 2.24 eV (564 nm) and 3.10 eV (400 nm) respectively,[2,42] still below the energy cutoff our solar simulator (290 nm). Even though the band gap energies of ZnO and TiO_2 are similar, the removal of chemisorbed nitrate from ZnO surface is significantly less. This lower reactivity is a consequence of two different effects: first, the chemisorbed nitrate coordination to the metal oxides, and second the formation of the nitrate salt $Zn(NO_3)_2$ by a neutralization process with ZnO rather than just a nitrate-oxide coordination such as the one observed on TiO_2. Significantly, the reaction of chemisorbed nitrate on γ-Al_2O_3 is analogous to that in aqueous nitrate, since γ-Al_2O_3 is a well known insulator.

Integration analysis of all nitrate bands shown in Figure 3A show that, with the exception of α-Fe_2O_3, chemisorbed nitrate follows an exponential removal with irradiation time, with the most significant nitrate reaction taking place within the first 90 minutes of irradiation. The chemisorbed nitrate removal from γ-Al_2O_3, TiO_2, SiO_2, and ZnO shows first order kinetics, with a heterogeneous photochemical rate constant, j, that can be expressed in the first order model as the integrated rate law

$$\frac{d[NO_3^-(a)]}{dt} = -j[NO_3^-(a)]$$

$$\therefore Ln\left(\frac{[NO_3^-(a)]}{[NO_3^-(a)]_0}\right) = Ln\left(\frac{\theta}{\theta_0}\right) = -jt \tag{5}$$

where $\left(\theta/\theta_0\right)$ is the ratio between the normalized absorption bands of chemisorbed nitrate at a given reaction time with respect of the absorption bands before the photochemical reaction. The reactant concentration decreases exponentially with time, with the initial coverage held constant. Since equation (5) establishes a ratio between the initial coverage (θ_0) and the coverage at any given time (θ), changes in the initial coverage should not result in an observable effect in the rate constant (j). Figure 4B shows the data fitted to a first order kinetic model in order to calculate the rate constant of the reaction. Table 1 summarizes the rate constant on each surface, along with the LOL, or the extent of the first order kinetics regime. All rate constants were determined within the linear section of equation (5), which was determined for each case as the limit of linearity with a 95% confidence of the data plotted in Figure 4B.[43] As summarized in Table 1 this limit of linearity (LOL) is different for each powder, and it determines the extent of the first-order kinetics. Recent heterogeneous photochemistry experiments with chemisorbed nitrates on γ-Al$_2$O$_3$ suggest a first order kinetics regime under 90 minutes.[23,10] Under our experimental conditions, the heterogeneous photochemistry of nitrates on γ-Al$_2$O$_3$ is first order for the first 54 $\pm$ 2 minutes. A photochemical rate constant of $j = (4.4 \pm 0.2)\times10^{-5}$ s^{-1} was calculated using equation (5) with data up to minute 54 of nitrate loss on γ-Al$_2$O$_3$, which is in good agreement with previously reported rate constants of chemisorbed nitrate photochemistry on γ-Al$_2$O$_3$.[23] In contrast with observations on γ-Al$_2$O$_3$, surface nitrate removal on TiO$_2$ takes place mainly within the first 24 minutes, and 74 minutes for ZnO. Panel B in Figure 4 corresponds to the first 50

minutes of the first-order kinetics reaction of all surfaces examined except α-Fe_2O_3, for which

nitrate loss was below our quantification limit. For all semiconductor oxides examined, the

heterogeneous photochemical rate constant derived from equation (5) and reported in Table 1, j,

is a combination of the photolysis rate constant of the adsorbed chromophore, j_{hv}, and the

semiconductor effect, j_e-, in the form of parallel reactions ($j = j_{hv} + j_e$-). However, the correlation

between semiconductor properties of the metal oxide and the heterogeneous photochemical rate

constant (j) is not direct, as both the photolysis rate (j_{hv}) and the semiconductor effect rate

constant (j_e-) closely depend on the coordination between nitric acid and metal oxide. In other

words, the photolysis rate constant and the semiconductor effect will not be the same for every

surface, as the substrate binds to the metal oxides with different coordination.

At the end of the linearity, as established in Table 1, the loss of chemisorbed nitrate was 15 ± 1

%, 10 ± 3 %, 7 ± 3 %, and 0.35 ± 0.09 %, for γ-Al_2O_3, TiO_2, SiO_2, and ZnO, respectively. The

fraction of nitrate loss during the first order reaction (R^I) is estimated comparing the yield at the

end the linearity (ϕ_{LOL}) with the yield near the end of irradiation time, 350 minutes, (ϕ_{350}):

$$R^1 = \frac{\phi_{LOL}}{\phi_{350}} \tag{6}$$

with R^I values of 0.55 ± 0.03, 0.56 ± 0.09 for γ-Al_2O_3 and TiO_2 respectively, and 0.8 ± 0.1 for

both SiO_2 and ZnO. Considering that first order kinetics nitrate yield (R^I) is above 0.5 for every

surface, surface nitrate loss predominantly goes through first order kinetics. However, the

photochemical reaction does not stop immediately after the first-order finished is reached, but

rather slows down until the nitrate loss cannot longer be detected.

The higher fraction of nitrates removed from γ-Al_2O_3, an insulator metal oxide, indicates that, while the semiconductor properties of the substrates are significant, the substrate coordination with the metal oxide also plays a relevant role in the photochemical reactivity of adsorbed nitrate. Conversely, semiconductor surfaces may lead to different oxidation states of products, as the electron-hole pair generated during a band-gap excitation can participate in the heterogeneous reaction, given that the electron-hole reaches enough chemical potential to induce a reaction. Therefore, an examination of the gas phase products in the context of the surface semiconductor properties is important.

3.3 Analysis of gas phase products. As indicated above, gas phase products detected were the same for all surfaces examined. Figure 5 shows the formation of the four main products detected during irradiation. The pressure of gas products was referenced to the absorbance of nitrate before broadband irradiation in order to account for variations in surface availability between experiments. The formation of gaseous products follows different kinetics for each gas detected, and an overall chemical kinetics different from that of the surface nitrate reaction producing them.
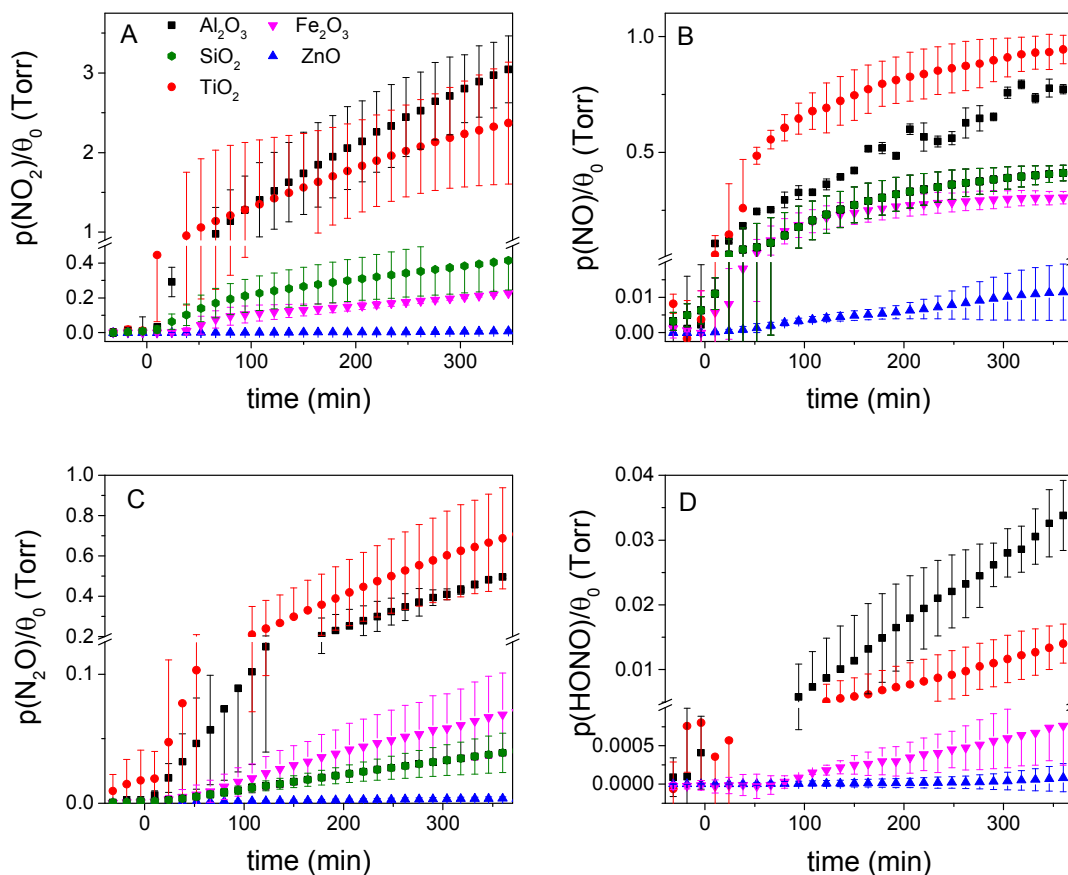
Figure 5. Gas-phase concentrations relative to initial nitrate coverage (θ_0) as a function of irradiation of time. Gaseous products from chemisorbed nitrate on five different surfaces are shown: α-Al_2O_3, TiO_2 (anatase), SiO_2, ZnO, and α-Fe_2O_3. Panel A shows the relative pressure of NO_2, panel B shows the relative pressure of NO, panel C shows the relative pressure of N_2O, and panel D shows the relative pressure of HONO. No quantifiable HONO band was measured during the SiO_2 irradiation.

As shown in Figure 5, NO_2 is the primary gaseous product in all reactions, with the exception of the reactions on ZnO, where NO is the primary product at the first order kinetic regime, with 2.5 ± 0.8 mTorr of pressure after 74 minutes of surface irradiation, while NO_2 and N_2O reached pressures of $(9 \pm 3) \times 10^{-4}$ $(5 \pm 1) \times 10^{-4}$ Torr, respectively, which corresponds to a 0.6 ± 0.2 NO

molar fraction as indicated in Table 2. Among the gaseous products, N_2O, NO_2 and HONO are photoactive in the UV-visible region. As shown in Figure 2, only the absorption cross-sections for NO_2 and HONO overlap with the radiation in the photochemical cell, while N_2O photolysis falls below the cutoff of the photochemical cell window.[28] Thus, only NO_2 and HONO can decay during their residence time (τ_{res}) in the photochemical cell, as they diffuse out of the irradiation region:

$$NO_2 + h\upsilon \xrightarrow{j_{NO_2}} NO + O \tag{7}$$

$$HONO + h\upsilon \xrightarrow{j_{HONO}} NO + OH \tag{8}$$

here j is the first order photolysis rate constant, which can be calculated using equation (9) for any gaseous product "p" from the overlap between the measured absolute irradiance and the known absorption spectral data:

$$j_p = \int_\lambda \sigma_p \phi_p I_S d\lambda \tag{9}$$

where σ_p and ϕ_p are the wavelength dependent absorption cross-section and dissociation quantum yield, respectively, for HONO or NO_2, and I_S is the spectral actinic flux for the broadband radiation determined from the data of Figure 2.[28,44] The rate constants calculated from equation (9) are $j_{NO2} \approx 2.6 \times 10^{-2}$ s^{-1} and $j_{HONO} \approx 3.9 \times 10^{-3}$ s^{-1}, higher than the atmospheric photolysis rate of 1.5×10^{-2} s^{-1} and 1.6×10^{-3} s^{-1} (at 0° zenith angle) for NO_2 and HONO, respectively,[14,45] which correlates with the fact that the radiation output from our solar simulator is higher, matching the irradiance at the top of Earth's atmosphere.

The only significant change in pressure in the reaction system is the result of product formation. Thus, products can be assumed to diffuse towards the gas chamber through low

pressures of the main product, NO_2. In order to evaluate the photolysis of NO_2 and HONO, the residence time, τ_{res}, of these gases in the region of irradiation is estimated from the diffusivity coefficient for a binary system at low pressures, with gases diffusing through NO_2, using equation (10), and NO_2 initially diffusing through air and then self-diffusing:

$$(\Delta x)^2_{avg} = 6D_{p-NO_2}\tau_{res} \tag{10}$$

where Δx is the average region of irradiation determined from the center of the irradiation region in Figure 2B, 2.75 cm, and D_{p-NO_2} is the diffusivity constant for the low pressure binary system of gas "p" through NO_2, determined with the Chapman and Enskog equation[46]

$$D_{A-NO_2} = \frac{2.66 \times 10^{-3}T^{3/2}}{P\,M_{p-NO_2}\,\sigma^2_{p-NO_2}\,\Omega_D} \tag{11}$$

with the molar mass $M_{p-NO_2} = 2[(1/M_p) + (1/M_{NO_2})]^{-1}$, Ω_D the diffusion collision determined with the Lennard-Jones energy, σ_{p-NO_2} the characteristic length from molecule "p" to NO_2, T is the reaction temperature of the reaction chamber, and P is the pressure of the system.[47] Thus, in order to minimize photolysis of gaseous photoactive products, the experimental conditions should follow equation (12), implying that the residence time must be smaller than the photolysis lifetime of product p, $\tau_p > \tau_{res}$:

$$\frac{1}{j_p} > \frac{(\Delta x)^2_{avg}}{6D_{p-NO_2}} \tag{12}$$

The diffusivity constant of NO_2 through air, calculated from equation (11), was $D_{NO2} = 1.0 \times 10^4$ Torr cm^2 s^{-1}, while HONO diffusivity has been estimated to be $D_{HONO} = 96$ Torr cm^2 s^{-1}.[48] Using these diffusion constants, the residence times at the end of the first order kinetics regime for γ-Al_2O_3 were calculated using equation (10), yielding τ_{res} values of approximately 14 ms and 15 ms for NO_2 and HONO, respectively. Thus, τ_{res} are smaller that their photolysis lifetimes,

calculated to be approximately 256 s and 39 s for NO_2 and HONO, respectively. Therefore, residence time does not allow enough time for significant photochemical reactions to occur during the first order kinetic regime. Furthermore, using τ_{res} as reaction time, the fraction of photoactive products reacted during their residence time in the photochemical cell, $[NO_2]_{\tau_{res}}/[NO_2]_0$, can be estimated assuming first order kinetics from equations (7) and (8)

$$\frac{d[NO_2]}{dt} = -j[NO_2] \Longrightarrow Ln\left(\frac{[NO_2]_{\tau_{res}}}{[NO_2]_0}\right) = -j \cdot \tau_{res}$$

$$\frac{[NO_2]_{\tau_{res}}}{[NO_2]_0} = e^{-j \cdot \tau_{res}} \tag{13}$$

Since, under our experimental conditrions $[NO_2]_{\tau_{res}}/[NO_2]_0 \cong 0.999$, there is no measurable photochemical decay of products during their residence time in the photochemical cell.

The kinetic difference in gas product formation observed in Figure 5 comes from two different aspects of the reaction: first, gaseous products formed during photochemistry of chemisorbed nitrate can undergo further reaction on the surface; for instance, nitrous oxide (N_2O) and NO_2 can be formed as shown in reaction (14):[38,39]

$$3NO \longrightarrow N_2O_2 + NO \longrightarrow N_2O(g) + NO_2(g) \tag{14}$$
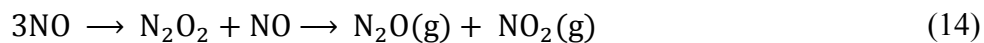
This subsequent reaction leads to more complex chemical kinetics than observed in the surface phase. While reaction (14) has been proposed as a gas-phase reaction, it can be a surface promoted reaction through adsorbed and/or re-adsorption of NO (*vide infra*). Second, heterogeneous photochemistry of chemisorbed nitrate may follow mechanisms that can lead to surface bound products. For example, the initial reduction of nitrates leading to surface bound NO_2^-, as indicated in reaction (2), or even further reduction to produce adsorbed NO^-.[9,23]

Alternatively, recent studies suggest the formation of N_2O by reaction of HONO (reaction 15), which is consistent with the steady growth of HONO and N_2O observed in Figure 5. In general, the formation of HONO is clearly observed during the photolysis of adsorbed nitrate on every surface examined, although especially significant for γ-Al_2O_3 and TiO_2. As a consequence, higher N_2O is expected through this mechanism.

$$2HONO(g) \longrightarrow N_2O(g) + O_2(g) + H_2O(g) \qquad (15)$$
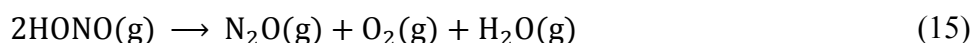
In addition, as Figure 5 illustrates, the amount of gas phase products also varies with the surface. Overall, the higher amount of gases are produced with irradiated adsorbed nitrate on γ-Al_2O_3 and TiO_2. The relatively small concentration of gas phase products from the irradiation on ZnO is in agreement with surface observation and supports the idea that most adsorbed nitrate has been converted into $Zn(NO_3)_2$ through neutralization. Table 2 summarizes the mole fraction of gas products at the limit of the first order kinetics regime (y^{LOL}) and near the end of the reaction at 350 minutes (y^{350}). For the two insulator metal oxides examined, γ-Al_2O_3 and SiO_2, the main product was NO_2 both during the first-order kinetic regime and at the end of the irradiation period.

Table 2. Molar fraction of gas-phase products during the predominantly first order kinetics (y^{LOL}) and molar fraction after 350 minutes of broadband irradiation (y^{350}). Data presented are averages of triplicate measurements.

Surface	y^{LOL}				y^{350}			
	$NO_2+N_2O_4$	NO	N_2O	HONO	$NO_2+N_2O_4$	NO	N_2O	HONO
γ-Al_2O_3	0.7 ± 0.1	0.3 ± 0.1	0.01 ± 0.01	0.001 ± 0.001	0.76 ± 0.01	0.19 ± 0.01	0.041 ± 0.003	0.008 ± 0.002
SiO_2	0.7 ± 0.2	0.3 ± 0.1	n/a	n/a	0.3 ± 0.09	0.5 ± 0.09	0.020 ± 0.005	n/a
TiO_2	0.5 ± 0.2	0.4 ± 0.2	0.09 ± 0.04	< 0.01	0.45 ± 0.03	0.44 ± 0.09	0.08 ± 0.04	0.004 ± 0.003
ZnO	0.2 ± 0.1	0.6 ± 0.1	0.136 ± 0.005	< 0.006	0.412 ± 0.001	0.51 ± 0.02	0.08 ± 0.02	< 0.005
α-Fe_2O_3	n/a	n/a	n/a	n/a	0.6 ± 0.2	0.4 ± 0.2	0.02 ± 0.01	0.008 ± 0.008

For the insulator surfaces, more reduced nitrogen oxide species, NO and N_2O, were found in relatively smaller proportion at the first-order kinetic regime. In fact, in the case of γ-Al_2O_3, N_2O can only be detected with confidence after the first order kinetics of the reaction has been completed. Similarly, for the insulators studied, HONO was only measured during nitrate irradiation on γ-Al_2O_3, although a small but clear HONO band was also observed during irradiation of chemisorbed nitrate on SiO_2, as can be seen in Figure 3B. Overall, as indicated in Figure 5, a significantly larger amount of gas product was detected from γ-Al_2O_3 than from SiO_2, which corresponds well with the amount of nitrate removed from each surface (Table 1).
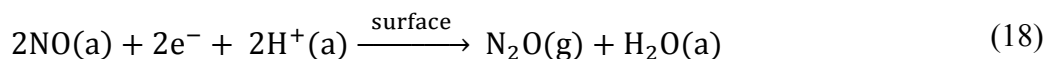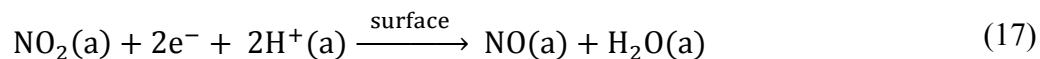
On the other hand, products obtained from nitrate chemisorbed on semiconductors show a relatively lower proportion of NO_2 and a relatively higher mole fraction of NO and N_2O at the end of the first order rate regime. This relative increase of N_2O formation suggests that surface semiconductive properties can affect surface mechanisms. While reduced nitrogen oxide species have also been detected on insulators, a recent work by Nanayakkara et al. on the surface photochemistry of adsorbed nitrate on α-Fe_2O_3 has shown further reduced surface bound species such as NO^-, suggesting a reducing effect of electrons in the oxide's conduction band.[9] The semiconductor metal oxides examined in this work, α-Fe_2O_3, TiO_2, and ZnO, have conduction band gaps measured in the visible to near UV spectral region. Therefore, irradiation of these metal oxides with photons having energies above their band gaps can create electron-hole pairs, which can initiate further photochemical reactions. In fact, the energy of electron-hole pairs on TiO_2 and ZnO is higher than that of α-Fe_2O_3, justifying not only the higher reactivity but also the higher proportion of reduced species such as NO upon irradiation of TiO_2 and ZnO.[49] Overall, the average oxidation state of products (Z_{ave}) can be calculated from the oxidation state of the

product (Z_{prod}) and the gas phase molar fraction at the first order kinetic regime (y^{LOL}) reported in Table 2 using equation (16):

$$Z_{ave} = \sum Z_{prod} \cdot y^{LOL} \tag{16}$$

which results in $Z_{ave} = 3.41$ for both insulator metal oxides, while the semiconductors TiO_2 and ZnO have a Z_{ave} of 2.89 and 2.14, respectively. An observed Z_{ave} higher in products formed on insulator surfaces than that on semiconductors supports the argument of a reducing effect of electrons in the oxide's conduction band and further formation of lower oxidation state nitrogen (in the form of NO) by the paired holes in the valence band.

The difference in Z_{ave} is attributed to electron in the conduction band of the semiconductor metal oxide. Major products like NO_2 and NO have been reported on the metal oxide surface, where the electrons in the conduction band of the semiconductor can further produce N_2O, as described in reactions (17) and (18):[50]

$$NO_2(a) + 2e^- + 2H^+(a) \xrightarrow{\text{surface}} NO(a) + H_2O(a) \tag{17}$$

$$2NO(a) + 2e^- + 2H^+(a) \xrightarrow{\text{surface}} N_2O(g) + H_2O(a) \tag{18}$$

where the electrons and the acid media are provided by the surface. The participation of surface induced electrons suggests that the paired hole in the valence band (h_{vb}^+) will be left available on the semiconductor metal oxide. These valence band holes can react further with adsorbed nitrates to form surface bound NO_3, which readily photolyzes to produce NO_x.[13,51,52]

$$NO_3^-(a) + h_{vb}^+ \longrightarrow NO_3(a) \tag{19}$$

$$NO_3(a) \xrightarrow{h\nu} NO(g) + O_2(g) \tag{20}$$

$$NO_3(a) \xrightarrow{h\nu} NO_2(g) + O(g) \tag{21}$$

Water produced in the reduction reactions (17) and (18) would not be detected under our experimental conditions. However, water vapor can also compete for surface adsorption sites and react with the available holes on the surface of the metal oxide, dissociating into hydroxyl radicals and protons.[13,53]

Finally, NO can act as the precursor to N_2O even on insulator surfaces, via a heterogeneous reaction.[49]

$$3NO(g) \xrightarrow{surface} N_2O(g) + NO_2(g) \tag{22}$$
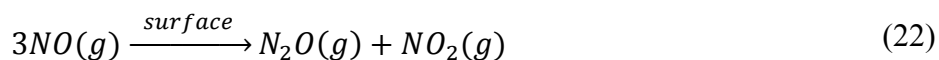
However, the higher proportion of N_2O from chemisorbed nitrates on semiconductor surfaces demonstrate that semiconductor components of atmospheric aerosols can trigger reducing reactions.[54, 55] There is a clear effect of the semiconductor properties of the surfaces examined in the heterogeneous photochemistry of chemisorbed nitrate, although a detailed mechanism for the reaction needs to be explored in future work. Overall, the reactivity of chemisorbed nitrate is a complex combination of adsorbed nitrate coordination and the semiconductor properties of the surface.

IV.   Conclusion

We have implemented a heterogeneous photochemistry experiment that incorporates the simultaneous investigation of both adsorbed HNO_3 and its gas phase products on various components of atmospheric aerosols. The system allows analysis in kinetically relevant time frames, as well as sample versatility, and low limits of detection of gas phase products. This work shows an exponential removal of chemisorbed nitric acid upon broadband irradiation, with characteristic first order kinetics, along with the formation of several nitrogen oxides and HONO

in the gas phase through alternative heterogeneous photolysis pathways. Therefore, daytime chemistry of chemisorbed nitrates can trigger alternative pathways for tropospheric renoxification. This heterogeneous photochemical reaction has surface dependent rate constants with each metal oxide leading to different yields. By contrasting semiconductor oxides, such as TiO_2, ZnO, and α-Fe_2O_3, with insulators, such as γ-Al_2O_3 and SiO_2, our results show that the photoactivity of the surface plays an important role in the production of reduced gaseous nitrogen oxides such as NO and N_2O.

Finally, this work shows that heterogeneous photochemistry of HNO_3 on tropospheric aerosol surfaces can have an impact in the chemical balance of the atmosphere. Even though these oxides are ubiquitous in the environment, the requirement of significant input of solar radiation makes heterogeneous photochemistry of nitrates more relevant on components of atmospheric aerosols. In particular, the oxides studied in this work might be in higher proportions in aerosols released into the atmosphere by combustion anthropogenic activities, such as fly ashes. As a consequence, the role of aerosol composition in heterogeneous photochemistry should be incorporated into current climate models to improve further the accuracy of atmospheric models.

Physical Chemistry Chemical Physics Accepted Manuscript

References

(1) Finlayson-Pitts, B. J. *Phys. Chem. Chem. Phys.* **2009**, *11*, 7760-7779.

(2) Chen, H. H.; Navea, J. G.; Young, M. A.; Grassian, V. H. *J. Phys. Chem. A.* **2011**, *115*, 490-499.

(3) Pandis, S. N.; Wexler, A. S.; Seinfeld, J. H. *J. Phys. Chem.* **1995**, *99*, 9646-9659.

(4) Gard, E. E.; Kleeman, M. J.; Gross, D. S.; Hughes, L. S.; Allen, J. O.; Morrical, B. D.; Fergenson, D. P.; Dienes, T.; M, E. G.; Johnson, R. J.; Cass, G. R.; Prather, K. A. *Science.* **1998**, *279*, 1184-1187.

(5) Nanayakkara, C. E.; Pettibone, J.; Grassian, V. H. *Phys. Chem. Chem. Phys.* **2012**, *14*, 6957-6966.

(6) Rubasinghege, G.; Elzey, S.; Baltrusaitis, J.; Jayaweera, P. M.; Grassian, V. H. *J. Phys. Chem. A. Letters* **2010**, *1*, 1729-1737.

(7) Finlayson-Pitts, B. J.; Raff, J. D.; Njegic, B.; Kamboures, M. A.; Chang, W.; Dabdub, D.; Gerber, R. B. *Abstr. Pap. Am. Chem. S.* **2009**, *237*, 177-177.

(8) Nie, W.; Wang, T.; Xue, L. K.; Ding, A. J.; Wang, X. F.; Gao, X. M.; Xu, Z.; Yu, Y. C.; Yuan, C.; Zhou, Z. S.; Gao, R.; Liu, X. H.; Wang, Y.; Fan, S. J.; Poon, S.; Zhang, Q. Z.; Wang, W. X. *Atmos. Chem. Phys.* **2012**, *12*, 11985-11995.

(9) Nanayakkara, C. E. J., Pradeep M.; Rubasinghege, G.; Baltrusaitis, J.; Grassian, V. H. *J. Phys. Chem. A.* **2013**, *118*, 158-166.

(10) Schuttlefield, J.; Rubasinghege, G.; El-Maazawi, M.; Bone, J.; Grassian, V. H. *J. Am. Chem. Soc.* **2008**, *130*, 12210-12211.

(11) Richards-Henderson, N. K.; Callahan, K. M.; Nissenson, P.; Nishino, N.; Tobias, D. J.; and Finlayson-Pitts, B. *Phys. Chem. Chem. Phys.* **2013**, *15*, 17636-17646.

(12) Knipping, E. M.; Dabdub, D. *Atmos. Environ.* **2002**, *36*, 5741-5748.

(13) Ndour, M.; Conchon, P.; D'Anna, B.; Ka, O.; George, C. *Geophys. Res. Lett*. **2009**, *36*, L05816.

(14) Seinfeld, J. H.; Pandis, S. N.: Atmospheric chemistry and physics: from air pollution to climate change; 2nd ed.; J. Wiley: Hoboken, N.J., 2006.

(15) Fung, I. Y.; Meyn, S. K.; Tegen, I.; Doney, S. C.; John, J. G.; Bishop, J. K. B. *Global Biogeochem. Cy*. **2000**, *14*, 281-295.

(16) Claquin, T.; Schulz, M.; Balkanski, Y. J. *J. Geophys. Res-Atmo*. **1999**, *104*, 22243-22256.

(17) Hoffmann, M. R.; Martin, S. T.; Choi, W. Y.; Bahnemann, D. W. *Chem. Rev.* **1995**, *95*, 69-96.

(18) Ivanov, V. P.; Kochubey, D. I.; Kutzenogii, K. P.; Bufetov, N. S. *React. Kinet. Catal. L.* **1998**, *64*, 97-102.

(19) Usher, C. R.; Michel, A. E.; Grassian, V. H. *Chem. Rev.* **2003**, *103*, 4883-4940.

(20) Mahowald, N. M.; Baker, A. R.; Bergametti, G.; Brooks, N.; Duce, R. A.; Jickells, T. D.; Kubilay, N.; Prospero, J. M.; Tegen, I. *Global Biogeochem. Cy.* 205, 19, GB4025.

(21) Linke, C.; Möhler, O.; Veres, A.; Mohácsi, A.; Bozóki, Z.; Szabó, G.; Schnaiter, M. *Atmos. Chem. Phys.* **2006**, *6*, 3315-3323.

(22) Hanisch, F.; Crowley, J. N. *Atmos. Chem. Phys*. **2003**, *3*, 119-130.

(23) Rubasinghege, G.; Grassian, V. H. *J. Phys. Chem. A.* **2009**, *113*, 7818-7825.

(24) Baltrusaitis, J.; Schuttlefield, J.; Jensen, J.; Grassian, V. *Phys. Chem. Chem. Phys*. **2007**, *9*, 4970-4980.

(25) Barney, W. S.; Wingen, L. M.; Lakin, M. J.; Brauers, T.; Stutz, J.; Finlayson-Pitts, B. J. *J. Phys. Chem. A.* **2000**, *104*, 1692-1699.

(26) Wingen, L. M.; Barney, W. S.; Lakin, M. J.; Brauers, T.; Finlayson-Pitts, B. J. *J. Phys. Chem. A.* **2000**, *104*, 329-335.

(27) Rajeshwar, K. *J. Appl. Electrochem.* **1995**, *25*, 1067-1082.

(28) Sander, S. P.; Friedl, R. R.; Golden, D. M.; Kurylo, M. J.; Moortgat, G. K.; Wine, P. H.; Ravishankara, A. R.; Kolb, C. E.; Molina, M. J.; Finlayson-Pitts, B. J.; Huie, R. E. Chemial Kinetics and Photochemical Data for Use in Atmospheric Studies Evaluation No. 15. Jet Propulsion Laboratory: Pasadena, **2006**

(29) Welch, R. M.; Coddens, E. M.; Navea, J. G. *Proceedings of the A&WMA Annual Conference*. 2012, 106.

(30) Goodman, A. L.; Bernard, E. T.; Grassian, V. H. *J. Phys. Chem. A.* **2001**, *105*, 6443-6457.

(31) Auroux, A.; Gervasini, A. *J. Phys. Chem.* **1990**, *94*, 6371-6379.

(32) Tanabe, K. Z.: Solid acids and bases; their catalytic properties; Kodansha Academic Press: Tokyo, New York, 1970.

(33) Hester, R. E.; Scaife, C. W. J. *J. Phys. Chem.* **1967**, *47*, 5253-5258.

(34) Kagann, R. H.; Maki, A. G. *J. Quant. Spectrosc. Ra*. **1983**, *30*, 37-44.

(35) Sobczynski, A.; Dobosz, A. *Pol. J. Environ. Stud*. **2001**, *10*, 195-205.

(36) Ertl, G. *Ber. Bunsen-Ges. Phys. Chem.* **1994**, *98*, 1413-1420.

(37) Roca, M.; Zahardis, J.; Bone, J.; El-Maazawi, M.; Grassian, V. H. *J. Phys. Chem. A.* **2008**, *112*, 13275-13281.

(38) Malecki, A.; Malecka, B. *Thermochim. Acta* **2006**, *446*, 113-116.

(39) Melia, T. P. *J. Inorg. Nucl. Chem*. **1965**, 27, 95-98

(40) Beaumont, S. K.; Gustaftson, R. J.; Lambert, R. M. *Chemphyschem*. **2009**, *10*, 331-333.

(41) El Zein, A.; Bedjanian, Y. *J. Phys. Chem. A.* **2012**, *116*, 3665-3672.

(42) Yoder, M. N. *IEEE T. Electron Dev*. **1996**, *43*, 1633-1636.

(43) Miller, J. N.; Miller, J. C.: Statistics and chemometrics for analytical chemistry; 5th ed.; Pearson Prentice Hall: Harlow, England; New York, 2005.

(44) Wall, K. J., Schiller, C. L., and Harris, G. W. *J. Atmo. Chem*. **2006**, 55(1), 31-54

(45) Demerjian, K. L., Schere, K. L. Peterson, J. T. *Adv. Environ. Sci. Tech*. **1980**. 10, 369-459.

(46) Poling, B. E., Prausnitz, J. M. and O'Connell, J. P. (**2001**). The Properties of Gases and Liquids, 5th Edn. McGraw-Hill, New York.

(47) Massman, W. J. *Atmos. Env*. **1998**. 32 (6), 1111-1127

(48) Tang, M. J., Cox, R. A., Kalberer, M. *Atmos. Chem. Phys*. **2014**, 14, 9233-9247.

(49) Rusu, C. N.; Yates, J. T. *J. Phys. Chem. B*. **2000**, *104*, 1729-1737.

(50) Berlier, G.; Spoto, G.; Ricchiardi, G.; Bordiga, S.; Lamberti, C.; Zecchina, A. *J. Mol. Catal. A-Chem*. **2002**, *182*, 359–366.

(51) Kebede, M. A.; Scharko, N. K.; Appelt, L. E; Raff, J. D. *J. Phys. Chem. Lett*. **2013**, 4, 2618−2623

(52) Gankanda, A.; Grassian, V. H. *J. Phys. Chem. C*. **2014**. DOI: 10.1021/jp504399a

(53) Du, J.; Keesee, R.; Zhu, L. *J. Phys. Chem. A*. **2014**. DOI: 10.1021/jp500913e

(54) Chen, H.; Nanayakkara,C. E.; Grassian, V. H. *Chem. Rev*. **2012**, 112, 5919−5948

(55) Neri, G.; Walsh, J. J.; Wilson, C.; Reynal, A.; Lim, J. Y. C.; Li, X.; White, A. J. P.; Long, N. J.; Durrant, J. R.; Cowan, A. *J. Phys. Chem. Chem. Phys*., **2015**, 17, 1562-1566